



# Enhanced piezoelectric polarization by subtle structure distortion to trigger efficient photocatalytic CO<sub>2</sub>RR

Xiaofeng Wang <sup>a</sup>, Jingwen Jiang <sup>a</sup>, Li Yang <sup>a</sup>, Qi An <sup>a</sup>, Qijun Xu <sup>a</sup>, Yongxin Yang <sup>a</sup>, Hong Guo <sup>a,b,\*</sup>

<sup>a</sup> International Joint Research Center for Advanced Energy Materials of Yunnan Province, Electron Microscope Center of Yunnan University, School of Materials and Energy, Yunnan University, Kunming 650091, China

<sup>b</sup> Southwest United Graduate School, Kunming 650092, China



## ARTICLE INFO

**Keywords:**  
Piezo-photocatalysis  
Structure distortion  
CO<sub>2</sub> reduction

## ABSTRACT

Achieving the goal of carbon neutralization using photocatalytic CO<sub>2</sub> reduction has garnered widespread attention. However, rapid bulk-charge recombination seriously impedes the further improvement of photocatalytic properties. In response, we propose a novel strategy to solve this limitation using enhanced piezoelectric polarized electric fields. Co<sub>3</sub>O<sub>4</sub> is introduced into NaNbO<sub>3</sub> by straightforward photo-deposition method, which causes the distortion of NbO<sub>6</sub> octahedron to alter the symmetry and boost the piezoelectricity. Meanwhile, the increased Co sites facilitate the adsorption of CO<sub>2</sub>, and reduce the reaction energy barrier. As a result, the Co<sub>3</sub>O<sub>4</sub>-modified NaNbO<sub>3</sub> nanocubes possess outstanding properties of CO<sub>2</sub> reduction under the synergy of ultrasound and visible light with the yield of CO about 4579.71 μmol g<sup>-1</sup>. Furthermore, the mechanism of piezo-photocatalytic CO<sub>2</sub> reduction is revealed in detail based on DFT, KPFM, and in-suit DRIFTS characterizations, thus providing guidance for the design of high-performance CO<sub>2</sub> photoreduction systems.

## 1. Introduction

Exploiting natural resources solar energy to drive photocatalytic reactions to convert CO<sub>2</sub> into clean fuels offers great prospects for sustainable energy development [1–4]. Unfortunately, photocatalytic CO<sub>2</sub> reduction always faces a serious issue of rapid photogenerated bulk-charge recombination, due to the limited photon energy absorbed by semiconductor photocatalysts [5,6]. Meanwhile, most of current modification strategies overwhelmingly focus on constructing heterogeneous structures, depositing noble metal and engineering for surface defects [7–11]. Though these previous works mainly investigated the inhibitory effect of surface charge recombination by semiconductor materials, cannot boost bulk-charge separation significantly. In fact, bulk-charge recombination is much faster than that of surface charge, which is the key reason for the unsatisfactory photocatalytic performance [12].

Presently, accelerating the bulk-charge separation by piezoelectric polarized electric field has been proven to be an available method [13, 14], which can be regulated by optimizing the piezoelectric properties, thus achieving high-efficiency separation of photogenerated bulk-charge [15,16]. Structural distortion engineering is a satisfactory

method to adjust the piezoelectricity of materials, because it can improve the local dipole moment and enhances the macroscopic polarization [17]. Importantly, the enhanced piezoelectric polarized electric field is able to effectively actuate the photoinduced charge to migrate in the opposite directions, so that more photogenerated e<sup>-</sup> - h<sup>+</sup> transfer to the photocatalyst surface to take part in redox reaction [5]. According to the latest reports [18–20] perovskite NaNbO<sub>3</sub> (NNO) exhibits a great advantage due to its unique crystal structure, including the angular shared octahedral unit network of [NbO<sub>6</sub>] and polarity heterogeneity of high-performance piezoelectric materials, which is conducive to enhancing the charge migration in the crystal [16,21,22]. Although it has been demonstrated to be a promising method in the domains of pollutant elimination and water splitting by photocatalysis, the limited piezoelectric field strength severely affects the efficiency of piezoelectric driven system in photocatalysis [23,24]. An anabatic structural distortion may improve the macroscopic polarization of perovskite NNO given its inherent polarity, and thus probably enhances piezoelectricity to boost piezo-photocatalytic CO<sub>2</sub> reduction. The current modification methods mainly concentrate on ionic replacement way, which utilizes the difference between ionic radii to promote structural distortion [17,21]. Nevertheless, it inevitably causes defects

\* Corresponding author at: International Joint Research Center for Advanced Energy Materials of Yunnan Province, Electron Microscope Center of Yunnan University, School of Materials and Energy, Yunnan University, Kunming 650091, China.

E-mail address: [guohong@ynu.edu.cn](mailto:guohong@ynu.edu.cn) (H. Guo).

in the crystal structure, leading to unnecessary carrier recombination [25]. Hence, satisfactorily regulating the piezoelectricity of piezoelectric semiconductor is a great challenge. Additionally, the synergistic mechanism of piezoelectric effect and photoelectric effect is unclear and needs further study deeply.

Herein, we design an innovative and available strategy for  $\text{CO}_2$  reduction via combining the piezoelectric and photoelectric effects as depicted in **Scheme 1**.  $\text{Co}_3\text{O}_4$  nanoclusters are successfully introduced on perovskite NNO by straightforward photo-deposition method, which results in local unbalanced coulomb force. As a result of the emerging micromechanical disturbance, it can promote structural distortion and contribute to the enhancement of intrinsic dipole moment, thus enhancing piezoelectric properties. A piezoelectric polarization is formed in the existence of mechanical energy vibration and an internal electric field is established in the NNO to generate polarization charges. The tilt of energy bands and the opposite-direction movement of negative and positive charges strengthen the catalytic reduction capacity on the NNO piezoelectric. Additionally, the introduction of  $\text{Co}_3\text{O}_4$  also expands the visible light response range. The increased Co sites enhance the adsorption for  $\text{CO}_2$ , and reduce the reaction barrier. Thus,  $\text{NaNbO}_3\text{-Co}_3\text{O}_4$  1 % (NNO-C 1 %) presents an excellent capacity for piezo-photocatalytic reduction of  $\text{CO}_2$ . Moreover, the mechanism of piezo-photocatalytic  $\text{CO}_2$  reduction is investigated in detail through DFT, KPFM and in-suit DRIFTS, which supplies a reference and new inspiration for the development and design of efficient piezo-photocatalytic system.

## 2. Experimental section

Chemicals, materials, the production of NNO, computational details, characterization and the control experiment of photocatalytic  $\text{CO}_2$  reduction are presented in [Supporting Information](#).

### 2.1. Synthesis of NNO-C

The photo-deposition of the  $\text{Co}_3\text{O}_4$  was achieved with  $\text{Co}(\text{NO}_3)_2\cdot 6\text{H}_2\text{O}$  as the precursor, and  $\text{NaIO}_3$  was employed as the electron acceptors. Typically, 0.5 g  $\text{NaNbO}_3$  powder was suspended in 100 mL  $\text{NaIO}_3$  solutions (0.01 M), then 5.27 mL  $\text{Co}(\text{NO}_3)_2\cdot 6\text{H}_2\text{O}$  solution (5 mg/mL) was added. The solution was exposed to ultrasound about 30 min and then stirred for 30 min. After 0.5 h photo-deposition under

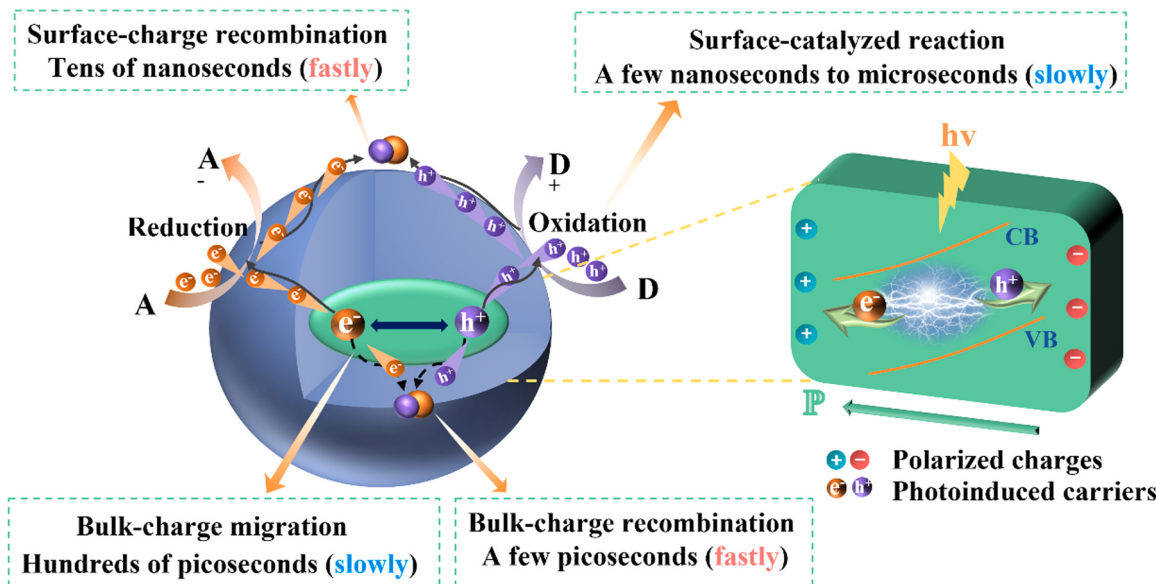
254 nm UV lamp, the obtained gray suspension was centrifuged three times with deionized water and ethanol solution and dried in a vacuum drying oven at 60 °C. The composite samples with the theoretical mass ratio of  $\text{NaNbO}_3$  and  $\text{Co}_3\text{O}_4$  at 5 % were obtained, and the as-prepared samples are denoted as NNO-C 5 wt%. The volume of  $\text{Co}(\text{NO}_3)_2\cdot 6\text{H}_2\text{O}$  solution was controlled to realize the preparation of NNO-C composites with different theoretical mass ratios. The actual content of  $\text{Co}_3\text{O}_4$  in NNO-C compound catalyst was measured by ICP, as shown in **Table S1**. According to the measured content, the composite samples are labeled as NNO, NNO-C 0.2 %, NNO-C 1 %, NNO-C 2.2 % and NNO-C 2.9 %, respectively.

### 2.2. Measurement of catalytic activity

The  $\text{CO}_2$  photoreduction on the photocatalysts in the presence of  $\text{H}_2\text{O}$  was conducted in the MCP-WS1000 Photochemical workstation (Beijing Perfectlight). The photocatalytic  $\text{CO}_2$  reduction was carried out in a 50 mL Pyrex reactor. Ultrahigh-purity  $\text{CO}_2$  (99.99 %) was fed continuously into the reactor at a rate of 0.1 L min<sup>-1</sup> to remove oxygen in the water and saturate the solution. 15 mg of sample was uniformly dispersed in the mixture of 20 mL deionized water, 19 mg ( $\text{Ru}(\text{bpy})_2(\text{CN})_2\text{Ru}(\text{bpy})(\text{COO})_2$ )<sub>22</sub> and 352 mg ascorbic acid by stirrer ( $\text{Ru}(\text{bpy})_2(\text{CN})_2\text{Ru}(\text{bpy})(\text{COO})_2$  is photosensitizer and ascorbic acid is sacrificial agent). Photocatalytic activities were investigated using a 300 W Xe lamp with a 420 nm cutoff filter (Perfect Light PLS-SXE 300) as the visible light source. A 300 W Xe light with a 420 nm cutoff filter was positioned 20 cm vertically above the photocatalytic reactor as a visible light source. An ultrasonic cleaner (KQ-600KDE, Kunshan) with frequency of 40 kHz and maximum power of 600 W was used to offer mechanical vibration. To avoid increasing of temperature induced by ultrasound, ice bags were placed to keep the temperature at 25 ± 1 °C. The gas product (0.5 mL, taken from the reactor) was analyzed using a GC-9790 Plus gas chromatograph equipped with a FID and a TCD detector (ZHE JIANG FULI ANALYTICAL INSTRUMENTS INC). Only the products of CO and  $\text{CH}_4$  were detected.

### 2.3. In-situ DRIFTS analyses for $\text{CO}_2$ photoreduction

In-situ DRIFTS (diffuse reflectance infrared Fourier transform spectra) tests were conducted on Nicolet iS50 FT-IR spectrometer (Thermo Fisher, USA) equipped with a designed reaction chamber and a



**Scheme 1.** Schematic diagram of photogenerated carrier recombination and redox reaction in photocatalyst, and scheme of photogenerated carrier separation enhanced by polarized electric field.

liquid water cool HgCdTe (MCT) detector. The sample along with a Cu holder was put into the reaction chamber. Then the sample was purged with  $N_2$  (30 mL/min) for 1 h to blow out all the gases in the cell and adsorbed on the samples. Then, the mixture of  $CO_2$  (5 mL/min) and  $H_2O$  vapor were introduced into the chamber for 30 min to make sure the sorption equilibrium before irradiation.

### 3. Results and discussions

#### 3.1. Theory calculation

In the light of most recent research findings, designing appropriate structural distortions in the structure of catalyst may offer an opportunity to increase the piezoelectric properties [16,26]. A suitable model for enhancing the efficiency of  $CO_2$  reduction by piezoelectric-assisted photocatalysis is provided by the structural distortion, which is induced by the  $Co_3O_4$  introduced into NNO and the increased piezoelectricity. To confirm the above prediction, the density functional theory (DFT) calculation was performed. The DOS in Fig. 1a, d indicates that the O 2p and Nb 4d orbitals, respectively, make up the majority of the

valence band (VB) and conduction band (CB) contributions. There are splitting waves DOS passing through the Fermi level ( $E_F$ ) and the  $E_F$  is located in the region where DOS is not zero, indicating that NNO is a semiconductor with strong metallic characteristics [27]. In comparison to NNO, the addition of  $Co_3O_4$  gives rise to an improved TDOS at the VB maximum. There are some Co 3d orbitals occupied by electrons in the region with higher energy than the O 2p orbitals, which may cause the band gap in NNO to become narrower, enhancing the capacity of electron transfer. In this instance, the  $e^-$  are easily transported to the CB and involved in the catalytic reaction after being photoinduced [28,29]. Besides, the spin-polarization DOSs of the CB and VB of NNO-C 1% are attributed to the introduction of magnetic  $Co_3O_4$  [30]. In contrast, spin-polarized DOS is not observed in pristine NNO, indicating the successful introduction of  $Co_3O_4$ .

In order to reveal the difference in polarity and cause of the differentiated piezoelectric response between NNO and NNO-C 1%, the dipole moments of materials and subtle variations of Nb-O bond length and angle in  $NbO_6$  octahedron have been assessed using DFT calculations. As illustrated in Fig. 1b, e, the introduction of  $Co_3O_4$  nanoclusters has subtly distorted the octahedral structure of  $NbO_6$ , resulting in the

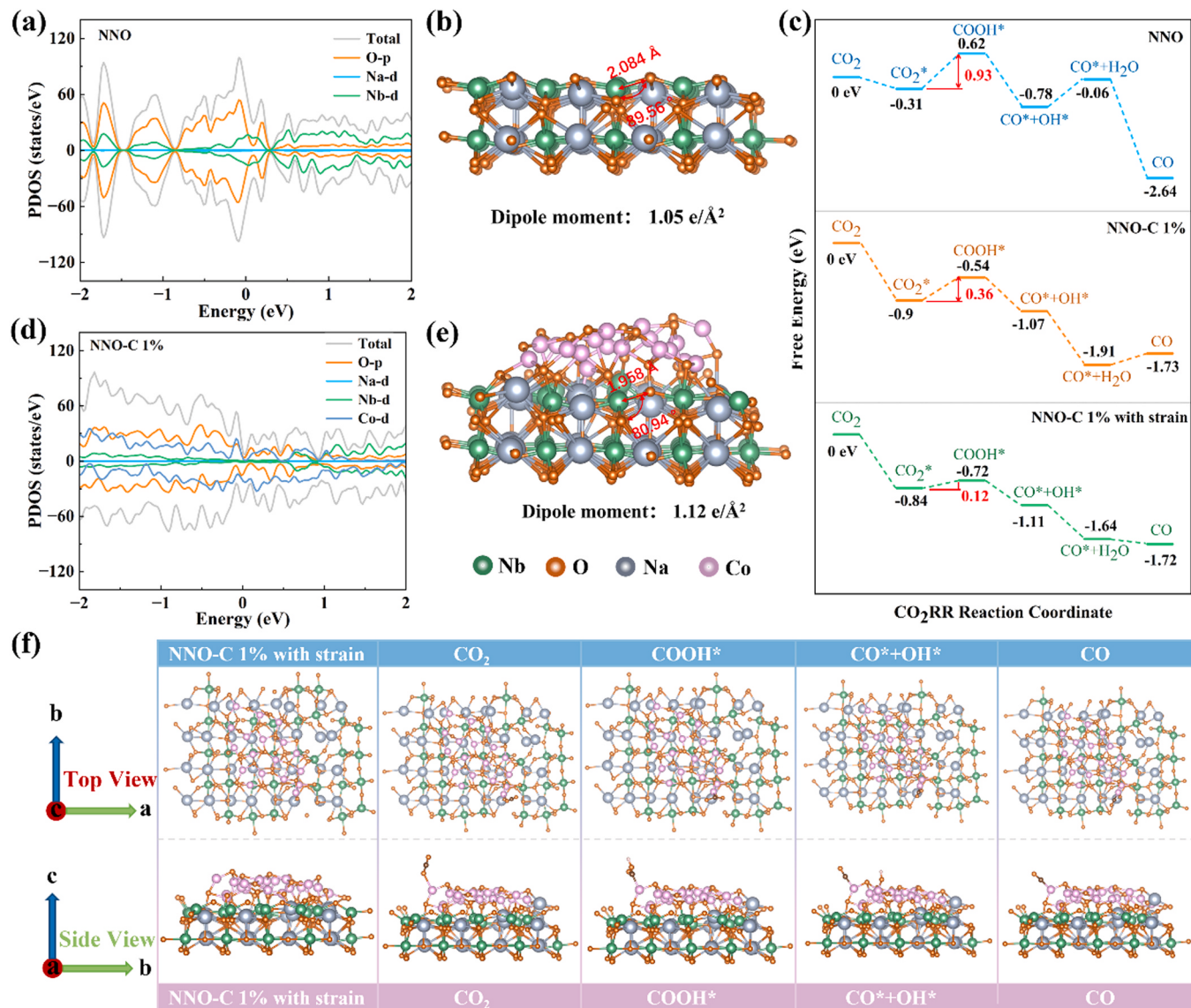


**Fig. 1.** (a) (d) The DOS spectra and (b) (e) the optimized geometric structures for NNO and NNO-C 1%. (c) The free energy of the main reactions during photo-catalytic reduction of  $CO_2$  for NNO, NNO-C 1% and NNO-C 1% in the case of applied strain. (f) The optimized geometric structures in the reaction path for NNO-C 1% with strain.

change of Nb-O bond length and bond angle from 2.084 Å, 89.56° to 1.058 Å, 80.94°. Intriguingly, the calculated dipole moment of NNO-C 1 % along the Z direction is 1.12 e/Å<sup>2</sup>, which is significantly higher than that of pure NNO (1.05 e/Å<sup>2</sup>). The findings indicate that the higher spontaneous polarization and greater piezoelectric responsiveness are caused by the distance among the negative and positive charge centers of NNO-C 1 %, which exhibits greater variation under mechanical strain in the direction of the asymmetry.

Additionally, to explore the promotion mechanism of  $\text{Co}_3\text{O}_4$  and piezoelectric polarization on the reaction thermodynamics, the most stable adsorption construction and energy of  $\text{CO}_2$  on the surface of NNO

and NNO-C 1 % are simulated by DFT. As presented in Fig. S1, the  $\text{CO}_2$  adsorption energy on NNO ( $-0.31$  eV) is found to be lower than that of NNO-C 1 % ( $-0.9$  eV) in the configuration with the most stable adsorption, indicating that the increased Co sites accelerate  $\text{CO}_2$  adsorption on NNO-C 1 % [31]. Further, Gibbs free energy ( $\Delta G$ ) calculations are deployed to evaluate the reaction free energy of every step in the  $\text{CO}_2$  photoreduction to  $\text{CO}$  process (Fig. 1c). The atomic configurations of the possible intermediates in the reaction path are presented in Fig. 1f and Fig. S2. The results show that generation of  $\text{COOH}^*$  is the limiting step for rate with the largest  $\Delta G$  ( $\Delta G_{\text{highest}}$ ). Significantly, NNO-C 1 % ( $\Delta G = 0.36$  eV) displays a much lower energy barrier for

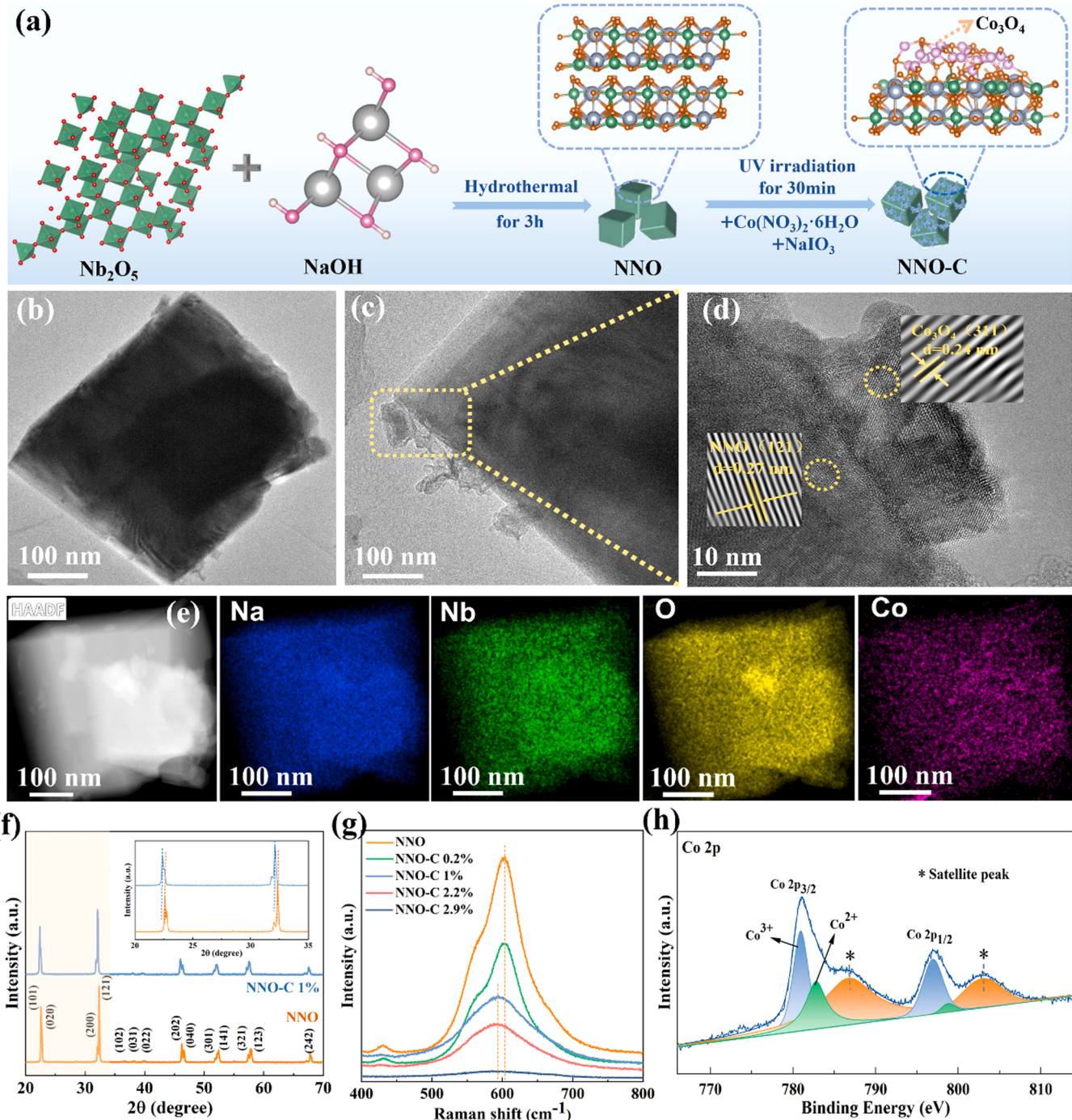


**Fig. 2.** (a) Schematic showing the synthesis of the NNO-C photocatalyst. (b)-(c) TEM images, (d) HRTEM image, and (e) elemental mapping images, Na (blue), Nb (green), O (yellow), Co (magenta) of NNO-C 1 %. (f) XRD spectra of NNO and NNO-C 1 %. (g) Raman spectra of NNO and NNO-C composites with different contents of  $\text{Co}_3\text{O}_4$ . (h) XPS spectrum of Co 2p for NNO-C 1 %.

COOH\* formation with respect to NNO ( $\Delta G = 0.93$  eV), proving that  $\text{Co}_3\text{O}_4$  can optimize the  $\text{CO}_2$  adsorption and activation on the catalyst surface and reduce the COOH\* formation energy, which is in favor of photocatalytic  $\text{CO}_2$  reduction reaction. Excitingly, by further introducing piezoelectricity, the enhanced internal piezoelectric effect in NNO-C 1 % can operate as a driving force to the effective separation of  $e^- - h^+$  pairs. The result exhibits the  $\Delta G_{\text{highest}}$  of NNO-C 1 % is decreased to 0.12 eV and the free energy curves become downhill. Thus, the piezoelectric polarization effect substantially diminishes the energy barrier of photocatalytic  $\text{CO}_2\text{RR}$ , which results in increased catalytic activity.

### 3.2. Morphology, architecture and chemical states

The synthesis scheme of NNO-C photocatalyst is depicted in Fig. 2a. Typically, the hydrothermal reaction of NaOH and  $\text{Nb}_2\text{O}_5$  produces NNO, and  $\text{Co}_3\text{O}_4$  nanoclusters were injected onto the surface of NNO by photo-deposition strategy. As shown in X-ray crystallography (XRD) spectra of the NNO and NNO-C (Fig. 2f and Fig. S3e), each diffraction peak is assigned to the orthorhombic crystal structure of the NNO, and no peak associated with  $\text{Co}_3\text{O}_4$  is discovered because there is a trace amount of  $\text{Co}_3\text{O}_4$  being introduced, proving well dispersion of  $\text{Co}_3\text{O}_4$  on the NNO surface. Nonetheless, the diffraction strength of each peak of NNO falls as  $\text{Co}_3\text{O}_4$  content rises and the peak position has shifted slightly to the left. This phenomenon is due to the addition of  $\text{Co}_3\text{O}_4$  resulting in the structural distortion of  $\text{NbO}_6$  octahedron and NNO crystallinity to reduce, which is in accord with DFT calculation results. Scanning electron microscope (SEM) images of pristine NNO are presented in Fig. S3a, which indicates that as-prepared NNO presents a cube structure. Fig. S3b displays clear lattice fringes belonging to NNO (101) crystal faces with a 0.39 nm spacing, which is in agreement with XRD measurements. A cubic shape for NNO is well maintained after  $\text{Co}_3\text{O}_4$  introducing, and the nanoclusters related to  $\text{Co}_3\text{O}_4$  were clearly observed on its surface (Fig. S3c-d and Fig. 2b-c). HRTEM in Fig. 2d displays identified lattice spacings of 0.24 nm for the (311) face of  $\text{Co}_3\text{O}_4$  and 0.27 nm for the (121) face of NNO, respectively. Besides, the Energy Dispersive Spectrometer (EDS) of NNO-C 1 % is shown in Fig. 2e. It is obvious that the elements Nb, Co, O, and Na are evenly distributed throughout the nanocubes. All the above phenomena directly suggest that  $\text{Co}_3\text{O}_4$  nanoclusters were successfully introduced into NNO. Furthermore, NNO-C exhibits paramagnetism due to the existence of spin state Co, so the introduction of  $\text{Co}_3\text{O}_4$  is further verified through electron paramagnetic resonance spectroscopy (EPR). As presented in Fig. S3f, the pure NNO spectrum has no unpaired electron signal. By clear contrast, because the  $e_g$  orbital in the spin state Co contains an unpaired electron, the NNO-C 1 % spectrum displays a prominent peak [32], which further supports the presence of the  $\text{Co}_3\text{O}_4$ .

Raman spectroscopy is used to further investigate the crystalline phase of the manufactured product since it is recognized as an effective technique for analyzing phase structures, space group and the short-range order for perovskites. As displayed in Fig. 2g, the stretched model of the Nb-O octahedron corresponds to the greatest band located close to  $600\text{ cm}^{-1}$ . The characteristic band moves toward a lower wavenumber and becomes noticeably broader as  $\text{Co}_3\text{O}_4$  content rises. The significant shift and broadening can be attributed to the introduction of  $\text{Co}_3\text{O}_4$  nanoclusters, which is in accord with the XRD and DFT calculation results. Additionally, it's well known that the Nb-O bond lengths for crystallized inorganic niobate substances are closely correlated with the Raman stretching shifts, and longer Nb-O bond lengths are consistent with lower wavenumber for the Raman stretching bands [33, 34]. As a result, the obvious shifts in Fig. 2g can be assigned to variations in the length of the Nb-O bond. According to study, the CB and VB of NNO are mostly generated via the Nb 4d and O 2p orbitals [35]. Hence, adjustment to the local structure of  $\text{NbO}_6$  octahedra, such as the change in bond lengths for Nb-O, may have an influence over the band structure of NNO, leading to variations in the optical band gap, which is in agreement with DFT calculations.

Brunauer-Emmett-Teller (BET) investigations have been performed to research the distribution of pore and specific surface area of NNO and NNO-C. As manifested in Fig. S4, the observed type IV  $\text{N}_2$  adsorption isotherms possess the characteristic of type H3 hysteresis loop [36]. Furthermore, the specific surface areas of NNO and NNO-C 1 % are 10.4 and  $11.4\text{ m}^2\text{g}^{-1}$ , respectively, exhibiting the specific surface areas of NNO is not changed considerably after the introduction of  $\text{Co}_3\text{O}_4$  nanoclusters. Aperture distribution data are obtained by BJH, which depict that there are numerous mesoporous structures in both NNO and NNO-C. Because mesoporous in principle is conducive to offering more catalytic active sites, boosting the transport of substances and charges, and facilitating the capture and adsorption of  $\text{CO}_2$ . Therefore, it will be in favor of the facilitation of photocatalytic capacity [36].

The X-ray photoelectron spectroscopy (XPS) is conducted to study the chemical constitution and elemental states of the catalysts. The total spectrum of NNO and NNO-C 1 % is displayed in Fig. S5a, demonstrating the existence of Na, Co, Nb, O elements in NNO-C 1 % and Na, Nb, O elements are greatly matched with that of pure NNO. The O 1 s XPS spectra are displayed in Fig. S5b, the three fitted peaks are allocated to the lattice oxygen of NNO, the surface adsorbed oxygen in -OH group and the oxygen in the chemisorbed  $\text{H}_2\text{O}$  molecule, respectively, with binding energies of 529.5 eV, 531.2 eV, and 533.8 eV [37,38]. As can be seen from the high-resolution XPS spectrum of Nb 3d in Fig. S5c, the two prominent peaks with spin orbits split to 2.7 eV, are located at 206.7 eV and 209.4 eV, which can be allocated to  $\text{Nb 3d}_{5/2}$  and  $\text{Nb 3d}_{3/2}$  of  $\text{Nb}^{5+}$  [39]. The great symmetry and narrow half-peak width of the two peaks indicate  $\text{Nb}^{5+}$  has a single valence state [18]. The XPS spectrum of Na 1 s is shown in Fig. S5d, where a fitted peak at 1071.2 eV proves the existence of  $\text{Na}^{+1}$ . Compared with the XPS spectra of each element in pure NNO, the peaks slightly move towards higher binding energy for NNO-C 1 % composite, which may be ascribed to the strong interaction between  $\text{Co}_3\text{O}_4$  and NNO leading to the change of Fermi energy level in NNO [40], as displayed in Fig. S6. The Co 2p XPS spectrum is illustrated in Fig. 2h, it is possible to identify the two peaks at 782.8 eV and 780.9 eV as  $\text{Co 2p}_{3/2}$  of  $\text{Co}^{2+}$  and  $\text{Co}^{3+}$ , respectively, and the two peaks around 798.8 eV and 796.9 eV belong to  $\text{Co 2p}_{1/2}$  [41]. According to the  $\text{Co}^{2+}$  and  $\text{Co}^{3+}$  fitted Co 2p spectra,  $\text{Co}^{2+}$  is partially oxidized to  $\text{Co}^{3+}$ , revealing  $\text{Co}_3\text{O}_4$  nanoclusters are successfully deposited on NNO. Meanwhile, the satellite peaks of  $\text{Co 2p}_{3/2}$  and  $\text{Co 2p}_{1/2}$ , respectively, are the two peaks at 787.3 eV and 802.6 eV [42,43]. According to reports, a spin-orbit splitting energy of 15.1–25.3 eV identifies the mixed-valence  $\text{Co}_3\text{O}_4$  [41]. Considering that the spin-orbital splitting energy of Co 2p in this case is 15.3 eV, hence it is also possible to draw the conclusion that  $\text{Co}_3\text{O}_4$  nanoclusters are successfully introduced into the NNO sample. Moreover, Fig. S5e depicts the relationship between magnetization and the magnetic field (M-H) curves. The enhanced magnetic properties of NNO-C 1 % following the introduction of  $\text{Co}_3\text{O}_4$  are confirmed by the M-H curve, and the distinct difference in magnetic behavior between the virgin NNO and NNO-C 1 % also confirms the successful introduction of  $\text{Co}_3\text{O}_4$  [44].

### 3.3. Catalytic activity

The piezocatalytic, photocatalytic, and piezo-photocatalytic  $\text{CO}_2$  reduction was conducted under ultrasonic vibration, visible irradiation, and the combined effects of ultrasound and irradiation, respectively, in the cause of validating the impact of polarized electric field on carrier separation in NNO-C. As illustrated in Fig. 3a-b, the pure NNO exhibits minimal photocatalytic CO and  $\text{CH}_4$  productivity, which can be assigned to the quick recombination of  $e^- - h^+$  pairs. Fascinatingly, the photocatalytic activity of NNO-C composites has been greatly boosted compared with NNO. The reason for the phenomenon could be due to the  $E_g$  narrowing of NNO, increased absorption of visible light and the increased Co sites, which enhances the  $\text{CO}_2$  adsorption, and reduces the reaction barrier following the introduction of  $\text{Co}_3\text{O}_4$ . Among them, when the amount of  $\text{Co}_3\text{O}_4$  exceeds 1 %, NNO-C composite

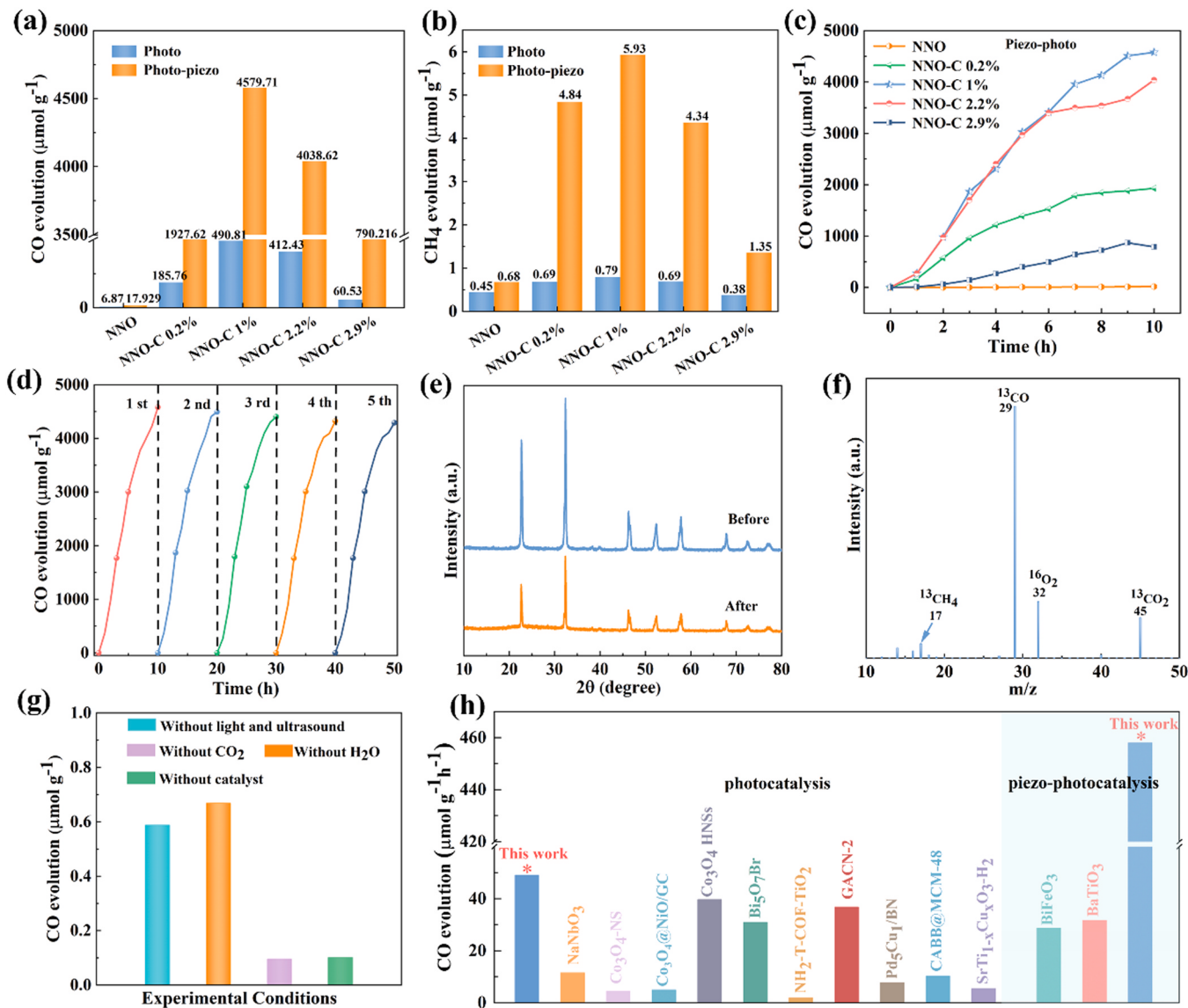


**Fig. 3.** The yield of (a) CO and (b) CH<sub>4</sub> of photocatalysis and piezo-photocatalysis for NNO and NNO-C samples with different contents of Co<sub>3</sub>O<sub>4</sub> in 10 h. (c) Alteration of the CO production rate by piezo-photocatalysis in 10 h for different catalyst. (d) Cycling tests of piezo-photocatalytic CO production of NNO-C 1 %. (e) XRD spectrum of NNO-C 1 % before and after 5 cycles of CO<sub>2</sub> piezo-photoreduction. (f) CH<sub>4</sub> and CO mass spectra produced in a <sup>13</sup>CO<sub>2</sub> ambience. (g) The yield of CO in controlled trial. (h) Comparison of CO-generating rate of NNO-C 1 % and some representative photocatalysts and piezoelectric catalysts.

photocatalysts show decreased photocatalytic activity. The shielding effect and unneeded recombination brought on by excessive Co<sub>3</sub>O<sub>4</sub> clusters could be the source of the occurrence. Significantly, the piezo-catalytic activity of NNO-C 1 % (CO: 4.95  $\mu\text{mol g}^{-1}$ , CH<sub>4</sub>: 0.46  $\mu\text{mol g}^{-1}$ ) is further improved by ultrasonic vibration alone than that of pristine NNO nanocubes (CO: 2.61  $\mu\text{mol g}^{-1}$ , CH<sub>4</sub>: 0.21  $\mu\text{mol g}^{-1}$ ) (Fig. S7). Although it has been demonstrated that the combination of NNO and Co<sub>3</sub>O<sub>4</sub> is conducive to the activity of piezocatalytic reactions, the modification is constrained due to the scarcity of carriers and recombination. Interestingly, the piezo-photocatalytic performances of all catalysts are considerably greater than that of alone photocatalysis or piezoelectric catalysis when visible light illumination and ultrasonic vibration are combined. The findings indicate that the CO and CH<sub>4</sub> generation rates of NNO-C 1 % are further increased to 4579.7  $\mu\text{mol g}^{-1}$  and 5.93  $\mu\text{mol g}^{-1}$  respectively, which is enhanced by nearly 10 times for CO production and nearly 8 times for CH<sub>4</sub> compared with that of light alone, indicating that piezoelectric polarization induced by ultrasound plays an essential role in increasing photocatalytic CO<sub>2</sub> reduction. This considerable improvement is mainly ascribed to the following two

facts: i) The energy band of NNO is tilted by the piezoelectric polarization produced by the ultrasound vibration energy, which also makes the reduction potential of CB more negative and enhances catalytic activity; ii) After the introduction of Co<sub>3</sub>O<sub>4</sub>, the enhanced piezoelectric polarization electric field triggered by ultrasonic vibration effectively boosts the transfer and separation of photoinduced carriers, which makes more e<sup>-</sup> and h<sup>+</sup> take part in the catalytic reaction in CO<sub>2</sub> reduction.

During the piezo-photocatalytic CO<sub>2</sub> reduction within 10 h, the generation of CO showed a steady increase trend (Fig. 3c). To demonstrate the steadiness of catalyst performance, we carried out a cycle test. As presented in Fig. 3d, the CO production only attenuated slightly after five cycles, indicating the catalyst has great stability. Moreover, XRD was performed on samples before and after the cycle, and the diffraction peaks of the XRD patterns are closely matched (Fig. 3e). This confirmed that the structure of NNO-C 1 % is not altered during the piezo-photocatalytic process, indicating that the catalyst is extremely stable, which is also the key factor in why it performs stable performance [45]. In order to clarify the sources of carbon in products and eradicate the

interference of polluting carbon during the process of preparation, the mass spectrometry experiment with isotope labeling was carried out under a  $^{13}\text{CO}_2$  atmosphere, proving that every carbon-based product is transformed from  $\text{CO}_2$  [46], as shown in Fig. 3f. Control experiments were carried out to confirm the necessary conditions of photocatalytic process and the detailed experimental procedures are provided in the Supporting Information. As displayed in Fig. 3g, CO content in the four controlled experiments could be ignored revealing that CO products were created by the piezo-photocatalytic reduction of  $\text{CO}_2$  in NNO-C 1 %, and any adjustment to the reaction conditions will significantly impact the activity. In addition, we made a synthetic comparison about catalytic reduction capability of  $\text{CO}_2$  by some previously reported piezoelectric and photocatalytic materials, the results exhibit that NNO-C 1 % has some of the best catalytic activity (Fig. 3h and Table S3), further indicating that the combination of  $\text{Co}_3\text{O}_4$  and NNO is advantageous for boosting catalytic reaction activity.

#### 3.4. Piezoelectric and photoelectrochemical properties

In general, the charge centers of the cations and anions can become

asymmetrical when external stress is in use for the surface of piezoelectrics. This will cause polarization and a built-in electric field, which drives the separation of photoinduced  $e^-$  and  $h^+$  pairs [47]. The piezoelectric properties of NNO and NNO-C 1 % are determined using piezoresponse force microscopy (PFM) and Kelvin probe force microscopy (KPFM). It is possible to clearly observe the surface structure of NNO and NNO-C in the topographic images (Fig. 4a), which is in agreement with the results of SEM and TEM images. The recognizable butterfly-shaped amplitude loops and phase curves indicate characteristic piezoelectric features of NNO and NNO-C composites under the bias voltage of  $\pm 5$  V and  $\pm 10$  V on the surface of catalysts (Fig. 4b–c and Fig. S8) [48]. Simultaneously, based on the slope of the amplitude loops, the maximum effective piezoelectric coefficient  $d_{33}$  has been determined in order to quantify the piezoelectric intensity quantitatively [49]. The effective piezoelectric coefficients  $d_{33}$  of NNO, NNO-C 0.2 %, NNO-C 1 %, and NNO-C 2.2 % are about 12.05, 21.61, 26.36, and 24.56  $\text{pm V}^{-1}$ , respectively. The results exhibit that the NNO-C composite has a stronger piezoelectric response signal with  $\text{Co}_3\text{O}_4$  contents increasing. Among them, when the amount of  $\text{Co}_3\text{O}_4$  exceeds 1 %, NNO-C composite photocatalysts show decreased piezoelectricity, which may be due to the

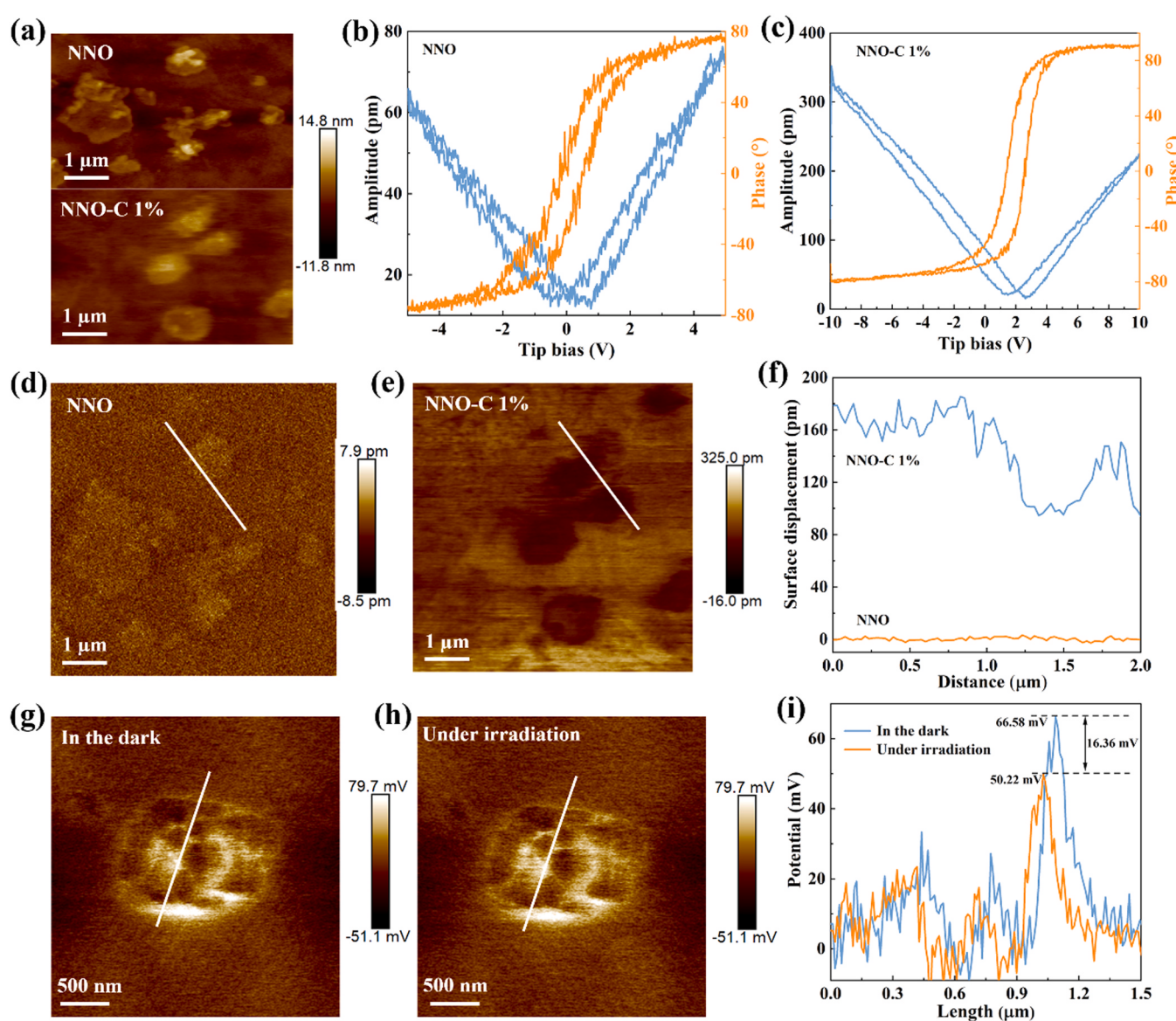


Fig. 4. (a) The topographic images, amplitude butterfly loops and phase curve of (b) NNO and (c) NNO-C 1 %. Amplitude images of (d) NNO and (e) NNO-C 1 %. (f) Surface height PFM spectra. KPFM potential images (g) in the dark and (h) under irradiation, and (i) surface potential spectra of NNO-C 1 %.

shielding effect caused by excessive  $\text{Co}_3\text{O}_4$  nanoclusters aggregating on the NNO surface. The decrease of piezoelectricity gives rise to the decrease of piezo-photocatalytic performance, which is consistent with the performance test results of  $\text{CO}_2$  reduction. The NNO-C 1% presents a higher piezoelectric response than NNO, which can be allocated to the distortion of the  $\text{NbO}_6$  octahedron that occurs in NNO following the

addition of  $\text{Co}_3\text{O}_4$ , resulting in stronger piezoelectric polarization and greatly increasing the piezoelectric effect. In Fig. 4d-f, the cross-sectional profile of the change from the surface displacement to the piezoresponse signal is shown for a more in-depth investigation. Intriguingly, the scan of NNO-C 1% displays an appreciable upward shift in comparison to the initial value of NNO, which demonstrates that

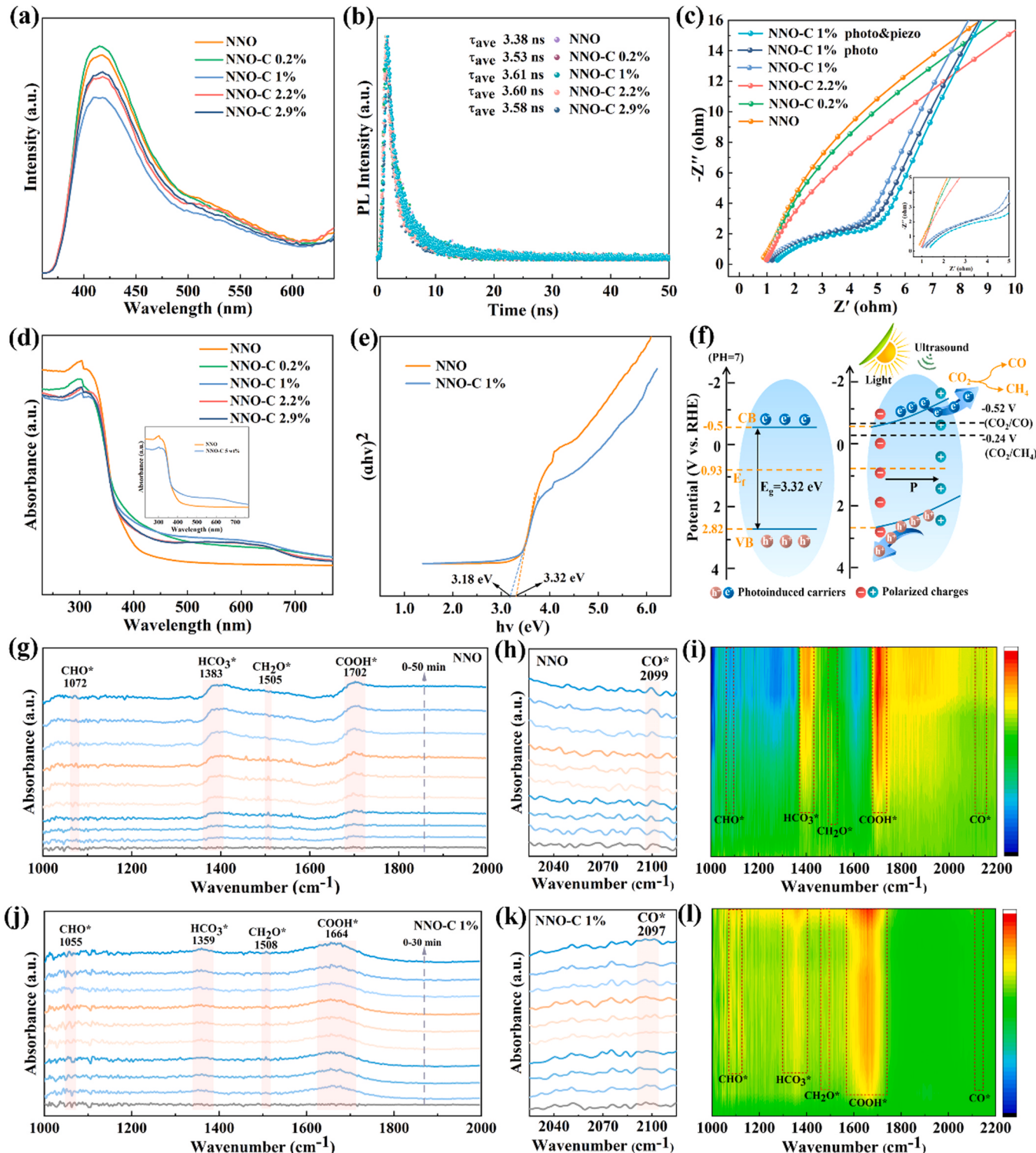


Fig. 5. (a) PL spectrum, (b) time-resolved PL decay spectrum and (d) UV-vis DRS of NNO and NNO-C samples with different contents of  $\text{Co}_3\text{O}_4$ . (c) EIS spectra of NNO and NNO-C samples with different contents of  $\text{Co}_3\text{O}_4$  under the illumination and ultrasound. (e) Band gap energy spectrum of NNO and NNO-C 1 %. (f) Band structure of NNO. The in-situ DRIFTS spectra for co-adsorption of a mixture of  $\text{CO}_2$  and  $\text{H}_2\text{O}$  on the (g)-(h) NNO and (j)-(k) NNO-C 1 %. Contour maps of the in-situ DRIFT of (i) NNO and (l) NNO-C 1 %.

the piezo-response signals of the entire domain and the domain wall are boosted. Consequently, the increased piezoelectric characteristic of NNO-C 1 % can produce more polarization charges when subjected to ultrasonic action, thus successfully accelerating surface redox processes. Furthermore, the potential at the surface of NNO-C 1 % catalyst is evaluated by KPFM under dark and irradiation. As presented in Fig. 4g-i, up to 66.58 mV of positive surface voltage is produced when the material is stressed by the probe tip, revealing the piezoelectric characteristic of catalyst [15]. Interestingly, the surface potential falls to 50.22 mV under light irradiation. The phenomenon can be allocated to the inherent electric field and the dipoles generated during charge migration in the sample [50], assisting in photogenerated  $e^-$  and  $h^+$  partially reduced the piezo-induced polarized charge, which is a sign that the built-in electric field is formed in the photocatalysts boosting the separation of photo-generated bulk-charge and enhancing photocatalytic activity.

The photoluminescence (PL), time-resolved PL decay and electrochemical impedance spectrum (EIS) Nyquist plots are performed to further investigate the transport characteristics of carriers for NNO and NNO-C. As displayed in Fig. 5a, at the 320 nm excitation wavelength, the emission peak appears at nearly 413 nm. The strength of peak corresponds to the recombination rate of photoinduced carriers. As expected, NNO-C 1 % presents the weakest peak intensity, and the photoluminescence intensity is obviously quenched, indicating that the combination of  $Co_3O_4$  and NNO can effectively impede the photo-generated carrier recombination. The lifetime of the photogenerated  $e^- - h^+$  pairs was characterized by the time-resolved PL decay spectra that were captured at the corresponding steady-state emission peaks, as manifested in Fig. 5b. In light of the findings of fitting, NNO-C 1 % has the longest carrier average lifetime ( $\tau_{ave} = 3.61$  ns), which suggests that the presence of  $Co_3O_4$  increases the efficiency of photoinduced carrier separation.

It is necessary to supply directly experimental evidence on enhancing the carrier separation efficiency via piezoelectric effect of  $Co_3O_4$ -modified  $NaNbO_3$  nanocubes. Hence, the transient photo-current test is carried out. As presented in Fig. S9, the results of transient photo-current responses illustrate that NNO-C composites exists the higher photocurrent density compared with pristine NNO, which means easier to separate and transfer carrier [51,52]. Generally, the rapid charge transfer between piezoelectric polarization charges and electroactive species is essential to fully participate in charge reactions. Therefore, NNO-C 1 % was further characterized by electrochemistry under ultrasonic vibration. Exhilaratingly, NNO-C 1 % exhibits a higher photocurrent density under ultrasonic vibration, demonstrating the enhanced carrier separation efficiency in the piezo-photocatalytic process. Moreover, to further explore the kinetics of charge transfer for the catalysts, EIS was conducted under visible light, ultrasound, and both at the same time. As illustrated in Fig. 5c, NNO-C 1 % shows the smallest arc radius than that of other samples. In general, the resistance for charge transfer is presented by the arc radius, and the decreased radius manifests the smaller resistance. That is, the quicker the photo-induced electron-hole pair separates and transfers. Therefore, NNO-C 1 % exhibits better photo-generated carrier separation performance. Interestingly, under the coupled action of ultrasound and irradiation, the arc radius of the EIS spectrum of NNO-C 1 % reduces, confirming that ultrasonic vibration energy offers a certain motive force for  $e^- - h^+$  pairs separation and transfer, resulting in enhanced catalytic performance.

The optical absorption capacities of the photocatalysts at different wavelengths are obtained using UV-Vis diffuse reflection spectroscopy (UV-Vis DRS). Fig. 5d depicts the UV-Vis absorption spectra with a 200–800 nm wavelength range, which indicates that the visible light response range of perovskite NNO is expanded by the addition of  $Co_3O_4$ . NNO-C 1 % exhibits the greatest ability to absorb visible light in the range of 430–740 nm. As the content of  $Co_3O_4$  increased,  $Co_3O_4$  nanoclusters started to gather, leading to the reduction in the absorption of visible light. According to the Tauc Plot method, the relation curve

between  $(\alpha h\nu)^2$  and  $h\nu$  gained by UV-vis absorption spectrum is manifested in Fig. 5e. The optical band gap values ( $E_g$ ) of NNO and NNO-C 1 % are 3.32 and 3.18 eV, respectively. The distortion of the NNO structure brought on by the addition of  $Co_3O_4$  results in a narrowing of the band gap, which is beneficial to facilitate the separation and transfer of photogenerated  $e^-$  and  $h^+$ .

In Fig. S10a, the Mott-Schottky curve has a positive slope, revealing that perovskite NNO is a N-type semiconductor, and its flat-band potential ( $E_{fb}$ ) is  $-0.7$  V vs Ag/AgCl ( $-0.5$  V vs NHE) [27]. Thus, the CB of NNO is estimated to be  $-0.5$  V. It is possible to deduce that VB is  $2.82$  V from the band gap value  $E_g$  (3.32 eV). The distance between VB and  $E_f$  may be calculated via VB-XPS (Fig. S10b), revealing the Fermi level  $E_f$  of NNO is  $0.93$  V, which is closer to CB and complies with the band structure of N-type semiconductors [53]. The energy band structure of NNO and principle of piezo-assisted photocatalysis is exhibited in Fig. 5f. Piezoelectric polarized electric field introduced by vibration energy boosts the transfer of photoinduced  $e^- - h^+$  in the opposite direction, thus effectively hindering their recombination. In addition, the band tilting caused by structural distortion makes the conduction potential of NNO more negative than the reduction potential of photocatalytic  $CO_2$  to  $CH_4$  and  $CO$  (Table S2), which distinctly enhances the photocatalytic capacity of  $CO_2$  reduction.

Furthermore, intermediates of  $CO_2$ RR process are tracked by in-situ DRIFTS under photocatalytic simulation to further research the mechanism of  $CO_2$  reduction via photocatalysis. As illustrated in Fig. 5g-l, the crucial intermediates for  $CO$  and  $CH_4$  formation such as  $COOH^*$  species are successfully discovered after applying photocatalytic reaction conditions [54,55], and the strength is enhanced as the extending of irradiation time. The inclusive  $Co_3O_4$  nanocluster NNO catalyst saturated the signal of  $COOH^*$  reaction intermediates faster with respect to pristine NNO, demonstrating that the introduction of  $Co_3O_4$  may accelerate the  $CO_2$  adsorption and activation by stabilizing the  $COOH^*$  reaction intermediates. In addition, the intermediates  $CHO^*$  and  $CH_2O^*$  formed by  $CH_4$  are not significantly detected, which indicates that  $CO^*$  groups generated on the photocatalyst surface are more prone to dissociate to produce  $CO$  gas, resulting in less  $CH_4$  production [56]. Compared with NNO, the bulge peak corresponding to  $COOH^*$  of NNO-C 1 % at  $1664\text{ cm}^{-1}$  was stronger, indicating that the introduction of  $Co_3O_4$  is more conducive to the formation and stabilization of intermediates for  $CO$  formation, which results in earlier  $CO$  generation time and higher concentration. The weak  $CO^*$  intermediates may be the result of rapid conversion [57]. These results reveal that NNO-C 1 % possesses improved photocatalytic  $CO_2$  reduction performance and increased  $CO$  selectivity, which is in line with the outcomes of the performance tests.

#### 4. Conclusion

In summary, NNO-C composite catalysts are successfully prepared by straightforward hydrothermal and photo-deposition methods, and combining the photoelectric effect with the piezoelectric effect to establish a novel kind of catalytic system. The introduction of  $Co_3O_4$  gains the effect of "killing two birds with one stone", which not only boosts the  $CO_2$  adsorption, reduces the reaction barrier, but also significantly enhances the piezoelectric polarization due to the subtle structural distortion. Besides, the experimental and electrochemical joint analysis indicates that the piezoelectric polarized electric field accelerates the separation and transfer of photoinduced bulk-charge and considerably improves the performance of reducing  $CO_2$ . The results exhibit that the yield of  $CO_2$  reduction to  $CO$  under piezo-photocatalysis of NNO-C 1 % is 255.4 times much higher than that of pure NNO. Moreover, the mechanism of piezo-photoreduction  $CO_2$  is thoroughly investigated by KPFM, in-suit DRIFTS and DFT calculation. This research offers a novel approach for achieving large-scale emission reduction and efficiently converting  $CO_2$  into clean fuels.

## Supporting information

Chemicals, materials, the synthesis of NNO and NNO-C, computational details, characterization and the experiment of photocatalytic CO<sub>2</sub> reduction and in-situ DRIFTS are presented in Supporting Information.

## CRediT authorship contribution statement

Xiaofeng Wang: Writing-original draft preparation. Jingwen Jiang: editing. Li Yang: methodology. Qi An: investigation. Qijun Xu: curation. Yongxin Yang: validation. Hong Guo: Research design, Funding supporting, Supervision.

## Declaration of Competing Interest

The authors declare that they have no known competing financial interests or personal relationships that could have appeared to influence the work reported in this paper.

## Data Availability

The authors do not have permission to share data.

## Acknowledgements

The authors acknowledge the support provided by the National Natural Science Foundation of Yunnan Province (202301AS070040), Scientific Research Foundation of Education Department of Yunnan Province (2023Y0266), Key Laboratory of Solid-State Ions for Green Energy of Yunnan University, Yunnan Key Laboratory of Carbon Neutrality and Green Low-carbon Technologies, the Electron Microscope Center of Yunnan University, MCP-WS1000 Photochemical workstation (Beijing Perfectlight), GC-9790 Plus gas chromatograph (ZHE JIANG FULI ANALYTICAL INSTRUMENTS INC), and the authors would like to thank Ting Li from Shiyanjia Lab ([www.shiyanjia.com](http://www.shiyanjia.com)) for the PFM analysis.

## Appendix A. Supporting information

Supplementary data associated with this article can be found in the online version at [doi:10.1016/j.apcatb.2023.123177](https://doi.org/10.1016/j.apcatb.2023.123177).

## References

- [1] Z. Sun, J. Fischer, Q. Li, J. Hu, Q. Tang, H. Wang, Z. Wu, M. Hankel, D. Searles, L. Wang, Enhanced CO<sub>2</sub> photocatalytic reduction on alkali-decorated graphitic carbon nitride, *Appl. Catal. B Environ.* 216 (2017) 146–155.
- [2] K. Wang, J. Lu, Y. Lu, C. Lau, Y. Zheng, X. Fan, Unravelling the CC coupling in CO<sub>2</sub> photocatalytic reduction with H<sub>2</sub>O on Au/TiO<sub>2</sub>-x: combination of plasmonic excitation and oxygen vacancy, *Appl. Catal. B Environ.* 292 (2021), 120147.
- [3] H. Chen, Y. Zhou, W. Guo, B. Xia, Emerging two-dimensional nanocatalysts for electrocatalytic hydrogen production, *Chin. Chem. Lett.* 33 (2022) 1831–1840.
- [4] Q. Xu, J. Jiang, X. Wang, L. Duan, H. Guo, Understanding oxygen vacant hollow structure CeO<sub>2</sub>@In<sub>2</sub>O<sub>3</sub> heterojunction to promote CO<sub>2</sub> reduction, *Rare Met.* 42 (2023) 1888–1898.
- [5] S. Tu, Y. Guo, Y. Zhang, C. Hu, T. Zhang, T. Ma, H. Huang, piezocatalysis and piezo-photocatalysis: catalysts classification and modification strategy, reaction mechanism, and practical application, *Adv. Funct. Mater.* 30 (2020) 2005158.
- [6] C. Hu, S. Tu, N. Tian, T. Ma, Y. Zhang, H. Huang, Photocatalysis enhanced by external fields, *Angew. Chem. Int. Ed.* 60 (2021) 16309–16328.
- [7] S. Liu, L. Chen, T. Liu, S. Cai, X. Zou, J. Jiang, Z. Mei, Z. Gao, H. Guo, Rich S vacant g-C<sub>3</sub>N<sub>4</sub>@CuIn<sub>5</sub>S<sub>8</sub> hollow heterojunction for highly efficient selective photocatalytic CO<sub>2</sub> reduction, *Chem. Eng. J.* 424 (2021), 130325.
- [8] M. Liang, T. Borjigin, Y. Zhang, B. Liu, H. Liu, H. Guo, Controlled assemble of hollow heterostructured g-C<sub>3</sub>N<sub>4</sub>@CeO<sub>2</sub> with rich oxygen vacancies for enhanced photocatalytic CO<sub>2</sub> reduction, *Appl. Catal. B Environ.* 243 (2019) 566–575.
- [9] L. Chen, T. Liu, S. Liu, S. Cai, X. Zou, J. Jiang, Z. Mei, G. Zhao, X. Yang, H. Guo, S vacant CuIn<sub>5</sub>S<sub>8</sub> confined in a few-layer MoSe<sub>2</sub> with interlayer-expanded hollow heterostructures boost photocatalytic CO<sub>2</sub> reduction, *Rare Met.* 41 (2022) 144–154.
- [10] Q. Liu, Y. Chai, L. Zhang, J. Ren, W. Dai, Highly efficient Pt/NaNbO<sub>3</sub> nanowire photocatalyst: Its morphology effect and application in water purification and H<sub>2</sub> production, *Appl. Catal. B Environ.* 205 (2017) 505–513.
- [11] S. Wang, X. Gu, X. Wang, X. Zhang, X. Dao, X. Cheng, J. Ma, W. Sun, Defect-engineering of Zr(IV)-based metal-organic frameworks for regulating CO<sub>2</sub> photoreduction, *Chem. Eng. J.* 429 (2022), 132157.
- [12] J. Li, L. Cai, J. Shang, Y. Yu, L. Zhang, Giant enhancement of internal electric field boosting bulk charge separation for photocatalysis, *Adv. Mater.* 28 (2016) 4059–4064.
- [13] Z. Luo, X. Ye, S. Zhang, S. Xue, C. Yang, Y. Hou, W. Xing, R. Yu, J. Sun, Z. Yu, X. Wang, Unveiling the charge transfer dynamics steered by built-in electric fields in BiOBr photocatalysts, *Nat. Commun.* 13 (2022) 2230.
- [14] H. Li, Y. Sang, S. Chang, X. Huang, Y. Zhang, R. Yang, H. Jiang, H. Liu, Z. Wang, Enhanced ferroelectric-nanocrystal-based hybrid photocatalysis by ultrasonic-wave-generated piezophotronic effect, *Nano Lett.* 15 (2015) 2372–2379.
- [15] C. Hu, F. Chen, Y. Wang, N. Tian, T. Ma, Y. Zhang, H. Huang, Exceptional cocatalyst-free photo-enhanced piezocatalytic hydrogen evolution of carbon nitride nanosheets from strong in-plane polarization, *Adv. Mater.* 33 (2021) 2101751.
- [16] M. Zhang, S. Nie, T. Cheng, Y. Feng, C. Zhang, L. Zheng, L. Wu, W. Hao, Y. Ding, Enhancing the macroscopic polarization of CdS for piezo-photocatalytic water splitting, *Nano Energy* 90 (2021), 106635.
- [17] Y. Wen, J. Chen, X. Gao, W. Liu, H. Che, B. Liu, Y. Ao, Two birds with one stone: cobalt-doping induces to enhanced piezoelectric property and persulfate activation ability of ZnO nanorods for efficient water purification, *Nano Energy* 107 (2023), 108173.
- [18] S. Zhang, B. Zhang, D. Chen, Z. Guo, M. Ruan, Z. Liu, Promising pyro-photo-electric catalysis in NaNbO<sub>3</sub> via integrating solar and cold-hot alternation energy in pyroelectric-assisted photoelectrochemical system, *Nano Energy* 79 (2021), 105485.
- [19] S. Singh, N. Khare, Flexible PVDF/Cu/PVDF-NaNbO<sub>3</sub> photoanode with ferroelectric properties: an efficient tuning of photoelectrochemical water splitting with electric field polarization and piezophotronic effect, *Nano Energy* 42 (2017) 173–180.
- [20] J. He, X. Wang, S. Lan, H. Tao, X. Luo, Y. Zhou, M. Zhu, Breaking the intrinsic activity barriers of perovskite oxides photocatalysts for catalytic CO<sub>2</sub> reduction via piezoelectric polarization, *Appl. Catal. B Environ.* 317 (2022), 121747.
- [21] H. Huang, S. Tu, C. Zeng, T. Zhang, A. Reshak, Y. Zhang, Macroscopic polarization enhancement promoting photo- and piezoelectric-induced charge separation and molecular oxygen activation, *Angew. Chem. Int. Ed.* 56 (2017) 11860–11864.
- [22] Z. Ren, F. Chen, Q. Zhao, G. Zhao, H. Li, W. Sun, H. Huang, T. Ma, Efficient CO<sub>2</sub> reduction to reveal the piezocatalytic mechanism: From displacement current to active sites, *Appl. Catal. B Environ.* 320 (2023), 122007.
- [23] C. Zhang, D. Lei, C. Xie, X. Hang, C. He, H. Jiang, Piezo-photocatalysis over metal-organic frameworks: promoting photocatalytic activity by piezoelectric effect, *Adv. Mater.* 33 (2021) 2106308.
- [24] K. Denault, J. Brögch, M. Gaultois, A. Mikhailovsky, R. Petry, H. Winkler, S. DenBaars, R. Seshadri, Consequences of optimal bond valence on structural rigidity and improved luminescence properties in Sr<sub>x</sub>Ba<sub>2-x</sub>SiO<sub>4</sub>:Eu<sup>2+</sup> orthosilicate phosphors, *Chem. Mater.* 26 (2014) 2275–2282.
- [25] Y. Zhang, N. Afzal, L. Pan, X. Zhang, J. Zou, Structure-activity relationship of defective metal-based photocatalysts for water splitting: experimental and theoretical perspectives, *Adv. Sci.* 6 (2019) 1900053.
- [26] Y. Liu, X. Hua, C. Xiao, T. Zhou, P. Huang, Z. Guo, B. Pan, Y. Xie, Heterogeneous spin states in ultrathin nanosheets induce subtle lattice distortion to trigger efficient hydrogen evolution, *J. Am. Chem. Soc.* 138 (2016) 5087–5092.
- [27] J. Jiang, X. Wang, Q. Xu, Z. Mei, L. Duan, H. Guo, Understanding dual-vacancy heterojunction for boosting photocatalytic CO<sub>2</sub> reduction with highly selective conversion to CH<sub>4</sub>, *Appl. Catal. B Environ.* 316 (2022), 121679.
- [28] L. Ran, Z. Li, B. Ran, J. Cao, Y. Zhao, T. Shao, Y. Song, M. Leung, L. Sun, J. Hou, Engineering single-atom active sites on covalent organic frameworks for boosting CO<sub>2</sub> Photoreduction, *J. Am. Chem. Soc.* 144 (2022) 17097–17109.
- [29] K. Li, Y. Cai, X. Yang, S. Wang, C. Teng, Y. Tian, Q. Min, W. Zhu, H<sub>2</sub>S involved photocatalytic system: a novel syngas production strategy by boosting the photoreduction of CO<sub>2</sub> while recovering hydrogen from the environmental toxicant, *Adv. Funct. Mater.* 32 (2022) 2113002.
- [30] C. Lin, T. Liu, S. Lin, K. Boopathi, C. Chiang, W. Tzeng, W. Chien, H. Hsu, C. Luo, H. Tsai, H. Chen, P. Kuo, J. Shieh, J. Chiou, W. Pong, C. Chen, C. Chen, Spin-polarized photocatalytic CO<sub>2</sub> reduction of Mn-doped perovskite nanoplates, *J. Am. Chem. Soc.* 144 (2022) 15718–15726.
- [31] J. Sheng, Y. He, J. Li, C. Yuan, H. Huang, S. Wang, Y. Sun, Z. Wang, F. Dong, Identification of halogen-associated active sites on bismuth-based perovskite quantum dots for efficient and selective CO<sub>2</sub>-to-CO photoreduction, *ACS Nano* 14 (2020) 13103–13114.
- [32] X. Kong, J. Ke, Z. Wang, Y. Liu, Y. Wang, W. Zhou, Z. Yang, W. Yan, Z. Geng, J. Zeng, Co-based molecular catalysts for efficient CO<sub>2</sub> reduction via regulating spin states, *Appl. Catal. B Environ.* 290 (2021), 120067.
- [33] K. Maeda, T. Mallouk, Comparison of two- and three-layer restacked Dion-Jacobson phase niobate nanosheets as catalysts for photochemical hydrogen evolution, *J. Mater. Chem.* 19 (2009) 4813–4818.
- [34] J. Wang, Z. Zou, J. Ye, Surface modification and photocatalytic activity of distorted pyrochlore-type Bi<sub>2</sub>M(M=In, Ga and Fe)TaO<sub>7</sub> photocatalysts, *J. Phys. Chem. Solids* 66 (2005) 349–355.
- [35] S. Park, H. Song, C. Lee, S. Hwang, I. Cho, Enhanced photocatalytic activity of ultrathin Ba<sub>5</sub>Nb<sub>4</sub>O<sub>15</sub> two-dimensional nanosheets, *ACS Appl. Mater. Interfaces* 7 (2015) 21860–21867.

[36] S. Wang, Y. Hou, X. Wang, Development of a stable  $\text{MnCo}_2\text{O}_4$  cocatalyst for photocatalytic  $\text{CO}_2$  reduction with visible light, *ACS Appl. Mater. Interfaces* 7 (2015) 4327–4335.

[37] S. Fujita, H. Kawamori, D. Honda, H. Yoshida, M. Arai, Photocatalytic hydrogen production from aqueous glycerol solution using  $\text{NiO}/\text{TiO}_2$  catalysts: effects of preparation and reaction conditions, *Appl. Catal. B Environ.* 181 (2016) 818–824.

[38] J. Liu, X. Li, R. Li, Q. Zhao, J. Ke, H. Xiao, L. Wang, S. Liu, M. Tadé, S. Wang, Facile synthesis of tube-shaped Mn-Ni-Ti solid solution and preferable Langmuir-Hinshelwood mechanism for selective catalytic reduction of  $\text{NO}_x$  by  $\text{NH}_3$ , *Appl. Catal. A-Gen.* 549 (2018) 289–301.

[39] P. Chen, W. Zhou, H. Zhang, Q. Pan, X. Zhang, B. Chu, Large thermal-electrical response and rectifying conduction behavior in asymmetrically reduced ferroelectric ceramics, *ACS Appl. Electron. Mater.* 1 (2019) 478–484.

[40] A. Nenning, A. Opitz, C. Rameshan, R. Rameshan, R. Blume, M. Hävecker, A. Knop-Gericke, G. Rupprecht, B. Klotzer, J. Fleig, Ambient pressure XPS study of mixed conducting perovskite-type SOFC cathode and anode materials under well-defined electrochemical polarization, *J. Phys. Chem. C* 120 (2016) 1461–1471.

[41] Z. Zhu, G. Lu, Z. Zhang, Y. Guo, Y. Guo, Y. Wang, Highly active and stable  $\text{Co}_3\text{O}_4/\text{ZSM-5}$  catalyst for propane oxidation: effect of the preparation method, *ACS Catal.* 3 (2013) 1154–1164.

[42] R. Li, H. Han, F. Zhang, D. Wang, C. Li, Highly efficient photocatalysts constructed by rational assembly of dual-cocatalysts separately on different facets of  $\text{BiVO}_4$ , *Energy Environ. Sci.* 7 (2014) 1369–1376.

[43] J. Liu, J. Ke, Y. Li, B. Liu, L. Wang, H. Xiao, S. Wang,  $\text{Co}_3\text{O}_4$  quantum dots/ $\text{TiO}_2$  nanobelt hybrids for highly efficient photocatalytic overall water splitting, *Appl. Catal. B Environ.* 236 (2018) 396–403.

[44] C. Cai, Y. Teng, J. Wu, J. Li, H. Chen, J. Chen, D. Kuang, In situ photosynthesis of an  $\text{MAPbI}_3/\text{CoP}$  hybrid heterojunction for efficient photocatalytic hydrogen evolution, *Adv. Funct. Mater.* 30 (2020) 2001478.

[45] J. Jiang, X. Zou, Z. Mei, S. Cai, Q. An, Y. Fu, H. Wang, T. Liu, H. Guo, Understanding rich oxygen vacant hollow  $\text{CeO}_2@\text{MoSe}_2$  heterojunction for accelerating photocatalytic  $\text{CO}_2$  reduction, *J. Colloid Interface Sci.* 611 (2022) 644–653.

[46] X. Wang, J. Jiang, Q. Xu, L. Duan, H. Guo, Understanding inclusive quantum dots hollow  $\text{CN}@$  $\text{CIZS}$  heterojunction for enhanced photocatalytic  $\text{CO}_2$  reduction, *Appl. Surf. Sci.* 604 (2022), 154601.

[47] S. Yuan, W. Io, J. Mao, Y. Chen, X. Luo, J. Hao, Enhanced piezoelectric response of layered  $\text{In}_2\text{Se}_3/\text{MoS}_2$  nanosheet-based van der waals heterostructures, *ACS Appl. Nano Mater.* 3 (2020) 11979–11986.

[48] D. Yu, Z. Liu, J. Zhang, S. Li, Z. Zhao, L. Zhu, W. Liu, Y. Lin, H. Liu, Z. Zhang, Enhanced catalytic performance by multi-field coupling in  $\text{KNbO}_3$  nanostructures: Piezo-photocatalytic and ferro-photoelectrochemical effects, *Nano Energy* 58 (2019) 695–705.

[49] C. Hu, H. Huang, F. Chen, Y. Zhang, H. Yu, T. Ma, Coupling piezocatalysis and photocatalysis in  $\text{Bi}_4\text{NbO}_8\text{X}$  ( $\text{X} = \text{Cl}, \text{Br}$ ) polar single crystals, *Adv. Funct. Mater.* 30 (2020) 1908168.

[50] A. Puthirath, X. Zhang, A. Krishnamoorthy, R. Xu, F. Samghabadi, D. Moore, J. Lai, T. Zhang, D. Sanchez, F. Zhang, N. Glavin, D. Litvinov, R. Vajtai, V. Swaminathan, M. Terrones, H. Zhu, P. Vashishta, P. Ajayan, Piezoelectricity across 2D phase boundaries, *Adv. Mater.* 34 (2022) 2206425.

[51] Y. Cheng, W. Ji, P. Hao, X. Qi, X. Wu, X. Dou, X. Bian, D. Jiang, F. Li, X. Liu, D. Yang, X. Ding, B. Han, A fully conjugated covalent organic framework with oxidative and reductive sites for photocatalytic carbon dioxide reduction with water, *Angew. Chem. Int. Ed.* (2023), e202308523 n/a.

[52] Y. Ma, X. Yi, S. Wang, T. Li, B. Tan, C. Chen, T. Majima, E.R. Waclawik, H. Zhu, J. Wang, Selective photocatalytic  $\text{CO}_2$  reduction in aerobic environment by microporous Pd-porphyrin-based polymers coated hollow  $\text{TiO}_2$ , *Nat. Commun.* 13 (2022) 1400.

[53] J. Jiang, X. Wang, H. Guo, Enhanced interfacial charge transfer/separation by LSPR-induced defective semiconductor toward high  $\text{Co}_2\text{RR}$  performance, *Small* (2023), 2301280.

[54] J. Yi, R. Xie, Z. Xie, G. Chai, T. Liu, R. Chen, Y. Huang, R. Cao, Highly selective  $\text{CO}_2$  electroreduction to  $\text{CH}_4$  by *in situ* generated  $\text{Cu}_2\text{O}$  single-type sites on a conductive MOF: Stabilizing key intermediates with hydrogen bonding, *Angew. Chem. Int. Ed.* 59 (2020) 23641–23648.

[55] Y. Wang, K. Wang, J. Meng, C. Ban, Y. Duan, Y. Feng, S. Jing, J. Ma, D. Yu, L. Gan, X. Zhou, Constructing atomic surface concaves on  $\text{Bi}_5\text{O}_7\text{Br}$  nanotube for efficient photocatalytic  $\text{CO}_2$  reduction, *Nano Energy* 109 (2023), 108305.

[56] X. Zhou, J. Shan, L. Chen, B.Y. Xia, T. Ling, J. Duan, Y. Jiao, Y. Zheng, S. Qiao, Stabilizing  $\text{Cu}^{2+}$  ions by solid solutions to promote  $\text{CO}_2$  electroreduction to methane, *J. Am. Chem. Soc.* 144 (2022) 2079–2084.

[57] X. Zhang, T. Liu, C. Liu, D. Zheng, J. Huang, Q. Liu, W. Yuan, Y. Yin, L. Huang, M. Xu, Y. Li, Z. Gu, Asymmetric low-frequency pulsed strategy enables ultralong  $\text{CO}_2$  reduction stability and controllable product selectivity, *J. Am. Chem. Soc.* 145 (2023) 2195–2206.